Acta Biomaterialia 149 (2022) 287–296

Contents lists available at ScienceDirect

Acta Biomaterialia

journal homepage: www.elsevier.com/locate/actbio

Full length article

A duplex-specific nuclease assisted photoelectrochemical biosensor based on MoS_2@ReS_2/Ti_3C_2 hybrid for ultrasensitive detection of colorectal cancer-related piRNA-31,143

Juan Li[a,1], Yao Tong[a,1], Zhiwei Sun[b], Yuqing Chen[a], Yunshan Wang[a], Lianqun Zhou[c], Yanyan Jiang[b,*], Peilong Li[a,*], Chuanxin Wang[a,d,e,*], Lutao Du[a,d,e,*]

[a] Department of Clinical Laboratory, The Second Hospital of Shandong University, Jinan, Shandong, China
[b] Key Laboratory for Liquid–Solid Structural Evolution and Processing of Materials, Ministry of Education, Shandong University, Jinan, Shandong, China
[c] CAS Key Lab of Bio-Medical Diagnostics, Suzhou Institute of Biomedical Engineering and Technology, Chinese Academy of Sciences, Suzhou, China
[d] Shandong Provincial Clinical Medicine Research Center for Clinical Laboratory, Jinan, Shandong, China
[e] Shandong Engineering & Technology Research Center for Tumor Marker Detection, Jinan, Shandong, China

ARTICLE INFO

Article history:
Received 10 February 2022
Revised 16 June 2022
Accepted 21 June 2022
Available online 25 June 2022

Keywords:
Photoelectrochemical sensor
Duplex-specific nuclease
piRNA
MoS2@ReS2 heterostructure

ABSTRACT

piR-31,143 has been identified as a potential biomarker for the diagnosis of colorectal cancer (CRC). However, the current detection methods have complicated operations and high cost, which restrict its clinical application. In the present work, we reported a new photoelectrochemical (PEC) biosensor based on MoS_2@ReS_2/Ti_3C_2 hybrid and duplex-specific nuclease (DSN) assisted signal amplification mechanism for ultrasensitive detection of piRNA-31,143 from human serum. The formation of the type I heterostructure between MoS_2 and ReS_2 and the doping of Ti_3C_2 contributed to high photocurrent response. The presence of piR-31,143 triggered the chain displacement reaction and enzymatic cyclic amplification reaction on the electrode surface with the assistance of DSN, leading to the collapse of the composite probe system. Consequently, the photocurrent of the PEC biosensor was proportional to the concentration of piR-31,143. The linear detection range and calculated detection limit of the PEC biosensor were 10^{-1}–10^{6} fM and 23 aM, respectively. The stability of the photocurrent under 15 consecutive on-off irradiations (with a relative standard deviation of 1.17%) and the specific response to piR-31,143 demonstrated the reliability of the PEC biosensor. In addition, the practicability of the PEC biosensor was verified by batch detection of human serum. The area under the receiver operating characteristic curve used to distinguish CRC patients from healthy controls was 0.942 with 100% specificity, demonstrating the developed method is a promising approach for the diagnosis of CRC.

Statement of significance

The clinical translation of piRNAs for cancer diagnosis is hindered by efficacy of detection techniques due to tedious sample processing and costly instrumentation. Herein, we fabricated a photoelectrochemical biosensor for the ultrasensitive detection of piR-31,143 with 10 μL serum in vitro. MoS_2@ReS_2/Ti_3C_2 greatly enhances the photocurrent response while duplex-specific nuclease improves the detection sensitivity and avoids false positives. By transforming the recognition sequence of the probe, the sensor can be applied to a variety of piRNAs detection for different diseases. In addition, the electrode can be recycled which is beneficial to reduce the cost of detection. With suitable automation and further optimization, our work may serve as core component in the development of an accurate and efficient diagnosis method.

* Corresponding author.
E-mail addresses: yanyan.jiang@sdu.edu.cn (Y. Jiang), lipeilong@whu.edu.cn (P. Li), cxwang@sdu.edu.cn (C. Wang), lutaodu@sdu.edu.cn (L. Du).
[1] Juan Li and Yao Tong contributed equally to this article.

https://doi.org/10.1016/j.actbio.2022.06.037

1. Introduction

PIWI-interacting RNAs (piRNAs) are the most recently discovered small non-coding RNAs with 24–31 nucleotides in length [1]. Studies have found that piRNAs exhibit abnormal expression patterns in body fluids of tumor patients and can be resistant to oxidation and degradation because of the 2′-O-methylation modification at their 3′-ends. piRNAs are a group of promising tumor markers [2–4], in particular, piR-31,143 has attracted much attention due to its function of regulating DNA methylation [5,6]. Its serum expression level could be used in the diagnosis of colorectal cancer (CRC), with an area under the receiver operating characteristic (ROC) curve (AUC) of 0.933 [7]. However, the traditional in vitro RNA detection techniques have some shortcomings, which restrict the clinical application of serum piR-31,143 in the diagnosis of CRC. As the standard of RNA detection, RT-qPCR requires tedious sample processing to remove inhibitory species and costly instrumentation [8,9]. RNA microarray can analyze multiple targets, while its sensitivity is relatively low [10]. Therefore, there is a need to develop low-cost, sensitive and convenient piRNA-based detection methods for disease diagnosis.

In recent years, biomedical quantification techniques using photoelectrochemical (PEC) sensors have been developed [11,12]. PEC sensors use light as the excitation source to excite photosensitive materials to produce an electrical signal as the output signal to achieve the detection of target molecules, which has the characteristics of low background signal and high sensitivity. Therefore, analysis with PEC sensors shows relatively higher performance than fluorescence method, electrochemiluminescence method, and other detection techniques [13,14].

The use of rhenium disulfide (ReS_2), as a member of the transition metal dichalcogenides (TMDs), has attracted increasing attention due to its unique anisotropic structure and direct bandgap from bulk to monolayer [15]. However, the rapid recombination of electron-hole pairs and poor electron transport capability of pure ReS_2 limits its wider application [16]. Molybdenum disulfide (MoS_2) is a two-dimensional (2D) graphene-like layered structure with a large active surface area that facilitates electron and hole transport [17–20]. It has the advantages of adjustable band gap, large carrier mobility, selective light detection ability, strong light material interaction, mechanical flexibility and environmental stability [21–24]. The combination of MoS_2 and ReS_2 has been studied for application in other fields [25–27]. We propose a type I MoS_2@ReS_2 heterojunction for the fabrication of PEC sensors, which is beneficial for separating the electrons and holes of the ReS_2 to effectively improve the carrier concentration and improve photoelectric conversion capacity. Furthermore, due to the high conductivity and carrier mobility, 2D Titanium Carbide (Ti_3C_2) can transfer the photo-generated electrons to the electrode immediately and inhibit the recombination efficiency of electrons and holes [28]. Therefore, assembling MoS_2@ReS_2 heterojunction and Ti_3C_2 into a new type of photosensitive material could provide a high-performance sensor.

Signal amplification is another important factor in improving detection sensitivity. Duplex-specific nuclease (DSN) is a thermostable enzyme isolated from the Kamchatka crab in recent years. It exhibits selective cleavage of double-stranded DNA (dsDNA) or DNA-RNA hybrids with more than 10–15 base complementary pairings, leaving the RNA strand intact during the cleavage [29,30]. When DNA probes are used in the RNA detection system, the presence of a target would trigger the chain displacement reaction and the enzymatic cyclic amplification reaction would occur with the assistance of DSN [31–33]. Compared with the standard PCR, the DSN-based isothermal detection method can directly detect RNA fragments without the need for reverse transcription and complex thermal cycling equipment, simplifying the design of specific primers and more suitable for in vitro detection.

In this study, we fabricated a new PEC biosensor based on MoS_2@ReS_2/Ti_3C_2 and established a DSN-assisted signal amplification system for the ultrasensitive detection of piR-31,143 in vitro (**Scheme 1**). The prepared biosensor had high conductivity and low hole electron-pair recombination efficiency, resulting in a strongly enhanced photocurrent response. DSN-based signal amplification strategy greatly improves the detection sensitivity and tellingly avoids false positives. Our current work provided a new way for designing various PEC sensors with high sensitivity.

2. Experimental section

Materials and characterizations of the materials were shown in the Supplementary Materials.

2.1. Preparation of Ti_3C_2, MoS_2, ReS_2 and MoS_2@ReS_2/Ti_3C_2 hybrid

Ti_3C_2 was prepared by hydrofluoric acid (HF) etching using Ti_3AlC_2 as the precursor. Briefly, 1.0 g of Ti_3AlC_2 was dispersed in 20 mL of HF and stirred at room temperature for 24 h. The suspension was filtered with ultrapure water until the pH reached 6. Layered Ti_3C_2 was obtained by vacuum drying at 60 °C for 12 h.

MoS_2, ReS_2 and MoS_2@ReS_2/Ti_3C_2 hybrid was prepared by one-step hydrothermal method. Briefly, materials were added to 30 mL of ultrapure water and the mixture was sonicated for 10 min. The solution was transferred to a Teflon-lined reactor and heated at 220 °C for 24 h. After the reactor was naturally cooled, the product was washed 3 times and obtained by vacuum drying at 60 °C for 12 h. The MoS_2 was fabricated by 0.1 mmol of $(NH_4)_6Mo_7O_{24}{\cdot}4H_2O$ and 1.4 mmol of CH_4N_2S. The ReS_2 was fabricated by 0.5 mmol of NH_4ReO_4 and 1.0 mmol of CH_4N_2S. MoS_2@ReS_2/Ti_3C_2 hybrid was prepared by 0.13 mmol of $(NH_4)_6Mo_7O_{24}{\cdot}4H_2O$, 0.73 mmol of NH_4ReO_4, 3.22 mmol of CH_4N_2S, and 0.2 g of Ti_3C_2.

2.2. Preparation of SiO_2-COOH

0.1 g of nano silica, 0.5 mL of (3-aminopropyl) triethoxysilane and 10 μL of triethylamine were ultrasonically dispersed in 15 mL of toluene and refluxed at 110 °C for 5 h. The refluxed product was washed with acetone and redispersed in 10 mL of ethanol. 10 mL of ethanol solution containing 0.5 g of glutaric anhydride was added dropwise to the above solution and stirred at 37 °C for 6 h. SiO_2–COOH was obtained after washing with ethanol and drying in air. SiO_2–COOH is ultrasonically dispersed in ultrapure water with a concentration of 2 mg/mL.

2.3. Fabrication of composite probe system

The composite probe system consisted of HS modified p1 and NH_2 modified p2. The sequences are shown in **Table S1**. An equimolar mixture of p1 and p2 was incubated at 37 °C for 90 min to obtain a p1-p2 solution at a concentration of 10 μM. Then, 100 μL of SiO_2–COOH solution, 5 mg of N–hydroxy succinimide, and 5 mg of N-(3-dimethylaminopropyl)-N'-ethyl carbodiimide hydrochloride were added to 1 mL of 10 mM MES buffer (pH 5.5) and stirred at 30 °C for 15 min. The solution was centrifuged and the sediment was redispersed in 1 mL of 10 mM Tris–HCl buffer (pH 7.4). The p1-p2 solution was then added and the mixture was stirred at 20 °C for 12 h. The composite probe system (SiO_2-p2-p1) was obtained by washing with ultrapure water three times. The final concentration of the composite probe system solution was 0.1 μM.

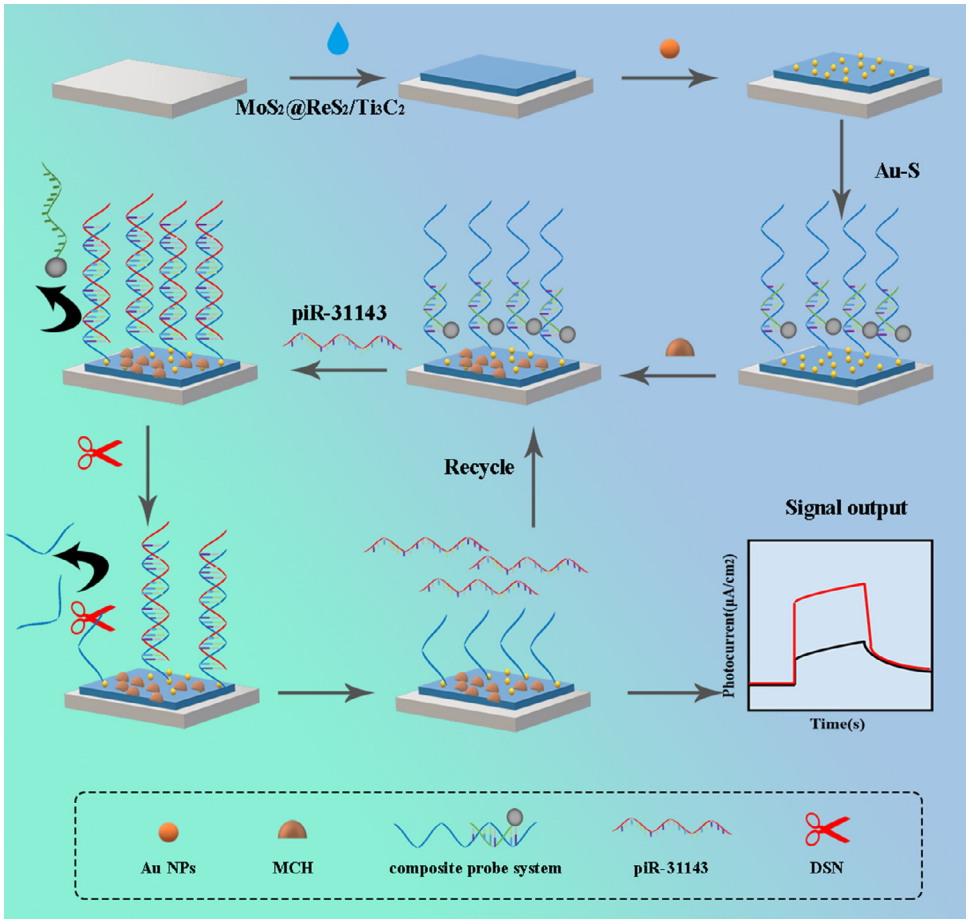

Scheme 1. Schematic diagrams of the fabrication and operation procedures of PEC biosensing platform for piR-31,143 detection.

2.4. Assembly of PEC sensing platform

The optimized conditions were obtained by comparing the photocurrent intensity of photochemical sensors under different conditions. Firstly, 10 μL MoS_2@ReS_2/Ti_3C_2 hybrid at a concentration of 4 mg/mL was added to a glassy carbon electrode (GCE) and dried at 25 °C for 4 h. Then gold nanoparticles (Au NPs) were electrodeposited on MoS_2@ReS_2/Ti_3C_2 Hybrid surface at a voltage of −0.2 V for 30 s with 1% $HAuCl_4$ as the electrolyte [34,35]. After rinsed with ultrapure water, 10 μL of composite probe system solution (0.1 μM) were added to the electrode and reacted at 4 °C for 12 h. Subsequently, the electrodes were rinsed with ultrapure water to remove the physical adsorption probes. Finally, 10 μL MCH at a concentration of 1 μM was added to the electrode surface, followed by reacting for 1 h to block the non-specific adsorption site.

2.5. Detection by the prepared PEC sensor

The PEC measurement was carried out on PEC workstation (DH7000, Jiangsu Donghua Analysis Instruments Co., Ltd., China) with a three-electrode system, which contained a 2 × 2 cm platinum counter electrode and an Ag/AgCl electrode reference electrode. The detection buffer was 0.01 M ascorbic acid (AA) solution, which was adjusted to pH 7.5 by Tris–HCl buffer (1 M, pH 9) and filled with nitrogen. The LED lamp served as the excitation light source and was switched off-on-off for 10 s-20 s-10 s under a potential of 0.15 V. The wavelength of the excitation light sources was 420 nm and the corresponding power was 170 W.

For piRNA analysis, the as-constructed biosensor was coated with 10 μL sample and incubated with 0.2 μL DSN and 1 μL 10 × DSN master buffer at 37 °C for 3 h. Next, 5 μL 2 × DSN Stop Solution (10 mM EDTA) was added to inactivate DSN. Finally, after rinsed with ultrapure water, the PEC measurement was performed in the AA buffer. Each sample was plotted with 3 repetitions. Electrochemical impedance spectroscopy (EIS) was recorded in the frequency range of 10 mV AC sine wave interfere with steady-state open-circuit voltage.

2.6. Statistical analysis

Statistical data of piR-31,143 level in serum samples were presented as median with interquartile range while others were presented as mean ± standard deviation (SD). Mann-Whitney test was used for comparison between two groups of data in serum samples from healthy controls and patients with colorectal cancer. All graphs were drawn by Origin 2021 and GraphPad Prism 9. The receiver operating characteristic curve (ROC) was drawn by MedCalc.

3. Results and discussion

3.1. Morphology and component characterization of photoactive material

Scanning electron microscopy (SEM) was employed to investigate the morphology and microstructure. In **Fig. 1A**, Ti_3C_2 presented an accordion-like appearance, indicating that the aluminum in Ti_3AlC_2 was corroded and Ti_3C_2 was successfully obtained [36]. In addition, the comparison of XRD pattern of Ti_3AlC_2 MAX phase and Ti_3C_2 showed the disappearance of (104) peak and the shift

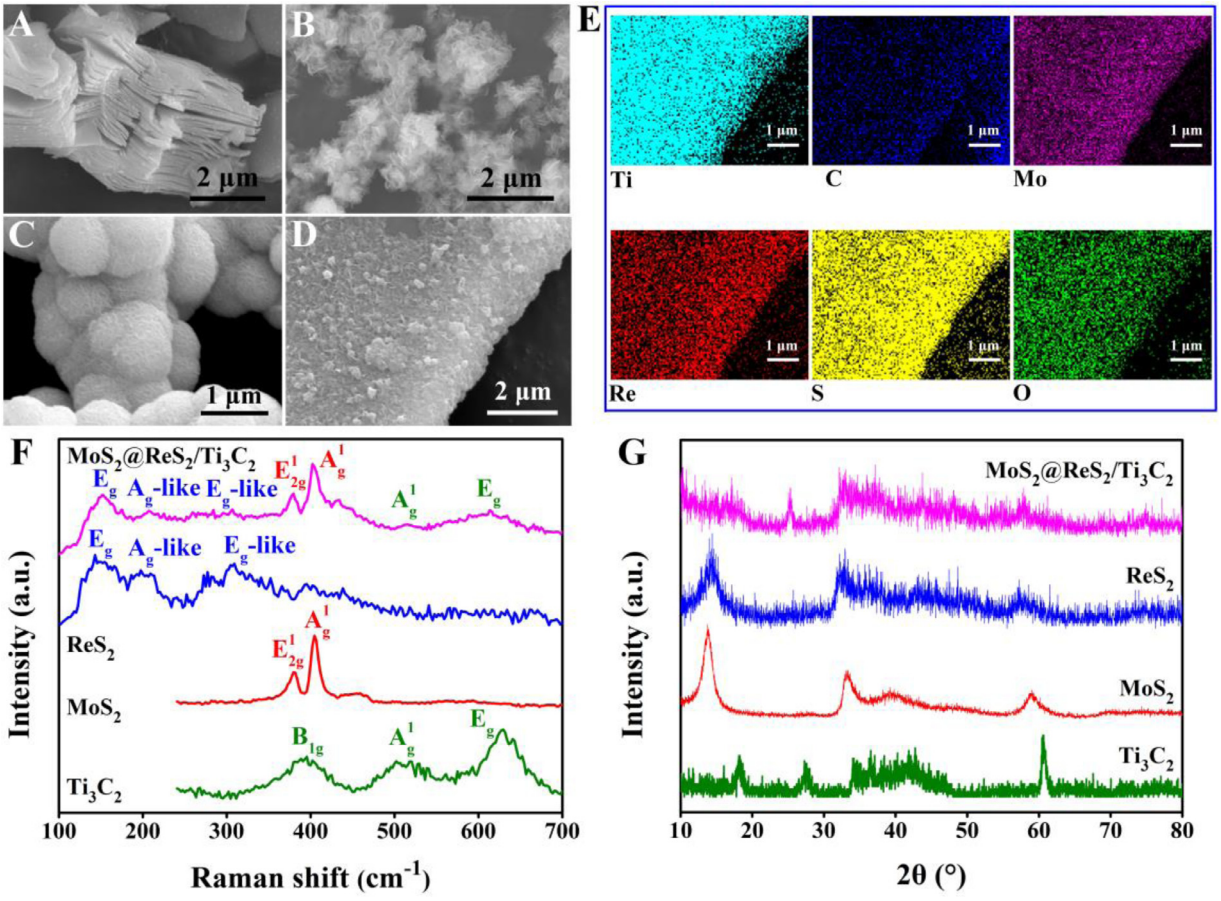

Fig. 1. Characterizations of Ti_3C_2, MoS_2, ReS_2 and MoS_2@ReS_2/Ti_3C_2. SEM images of Ti_3C_2 (A), MoS_2 (B), ReS_2 (C) and MoS_2@ReS_2/Ti_3C_2 hybrid (D). (E) Elemental mapping of MoS_2@ReS_2/Ti_3C_2 hybrid. Raman spectra (F) and XRD patterns (G) of Ti_3C_2, MoS_2, ReS_2 and MoS_2@ReS_2/Ti_3C_2 hybrid.

to a lower angle of (004) peak, indicating that the Al layers are successfully etched by HF (**Fig. S1**). MoS_2 showed an irregular nanoflower shape, while ReS_2 showed a spherical nanoflower shape [37] (**Fig. 1B** and **C**). The image in **Fig. 1D** illustrated that MoS_2@ReS_2 was loaded on the surface of the Ti_3C_2 nanosheet. EDS mapping images are shown in **Fig. 1E**, revealing that there appeared an even distribution of Ti, C, Mo, *Re*, S, and O across the structure of MoS_2@ReS_2/Ti_3C_2 hybrid, which verified the successful synthesis of nanostructure. The chemical structures of MoS_2, ReS_2, Ti_3C_2, and MoS_2@ReS_2/Ti_3C_2 were identified by Raman spectroscopy (**Fig. 1F**). The MoS_2@ReS_2/Ti_3C_2 hybrid displayed characteristic peaks of ReS_2 at 152 cm^{-1} (Eg), 208 cm^{-1}(Ag-like) and 306 cm^{-1}(Eg-like) [38], MoS_2 at 380 cm^{-1} (E^12g) and 405 cm^{-1} (A^1g) [39], Ti_3C_2 at 395 cm^{-1}(B1g), 515 cm^{-1} (Ag^1) and 628 cm^{-1}(Eg) [40], confirming the composition of the target structure. According to **Fig. 1G**, in the X-ray diffraction (XRD) pattern of the hybrid, four diffraction peaks appearing at 13.8°, 33.3°, 39.5°, and 58.5°, corresponding to the (002), (101), (103), and (110) crystal planes of MoS_2, respectively, were all retained [41]. The characteristic diffraction peaks at 14.4°, 32.9°, 37.4°, 43.2°, 57.9°, and 68.9° could be indexed to the (001), ($\bar{2}$01), (0$\bar{2}$2), ($\bar{2}$30) (2$\bar{4}$2) and (4$\bar{4}$1) planes of ReS_2, respectively [42]. Meanwhile, the characteristic peaks of Ti_3C_2 including (004), (101), (105), (107), (110) were retained in the MoS_2@ReS_2/Ti_3C_2 hybrid, indicating that the crystal structure was not changed.

The elemental composition and bonding state of the MoS_2@ReS_2/Ti_3C_2 hybrid were further explored by X-ray photoelectron spectroscopy (XPS) (**Fig. 2**). Results showed the existence of Ti, C, Mo, *Re*, S and O elements (**Fig. 2A**). The Ti 2p peaks at 457.3 and 463.0 eV demonstrated the presence of Ti-C (**Fig. 2B**). The electron binding energies of 283.3, 284.8 and 287.2 eV in the high-resolution XPS spectrum (**Fig. 2C**) of C 1 s were attributed to C-Ti, C–C, C–O, respectively. The Mo-S peaks of Mo 3d were about 227 eV (3d5/2) and 230.1 eV (3d3/2) (**Fig. 2D**) while the two peaks at 227.7 eV and 231 eV were related to Mo–O. The *Re* 4f-related XPS peaks for ReS_2 corresponded to *Re* $4f_{7/2}$ and *Re* $4f_{5/2}$ binding energies of Re^{4+} (**Fig. 2E**). The S 2p displayed two peaks attributed to S $2p_{3/2}$ and S $2p_{1/2}$ (**Fig. 2F**), respectively. Furthermore, the high-resolution XPS of O 1 s (**Fig. 2G**) showed three peaks corresponding to O-Ti, Mo-OH and *Re*-OH in the nanocomposite, which further demonstrated the effective synthesis of MoS_2@ReS_2/Ti_3C_2 hybrid.

3.2. Working mechanism

Fig. 3 shows the UV–Vis absorption spectra and Tauc plots of MoS_2 and ReS_2. MoS_2 had a band gap (E_g) of 1.43 eV and light absorption range to the infrared region (**Fig. 3A** and **B**). The E_g of ReS_2 was 1.84 eV according to the Tauc plot method, which made its wavelength absorption range cover the entire visible light (**Fig. 3C** and **D**). **Fig. 3E** shows the photocurrent generating mechanism of the proposed PEC biosensor. The positions of the conduction band (E_{CB}) and valence band (E_{VB}) of MoS_2 and ReS_2 were calculated according to the empirical formulas $E_{CB} = \chi - E_0 - 0.5E_g$ and $E_{CB} = E_{VB} - E_g$. χ represents the geometric mean of the absolute electronegativity of each atom of the semiconductor and the χ of MoS_2 is 5.32 while ReS_2 is 5.38. E_0 is the energy of free electrons on the hydrogen scale (~4.5 eV) [43]. Therefore, the calcu-

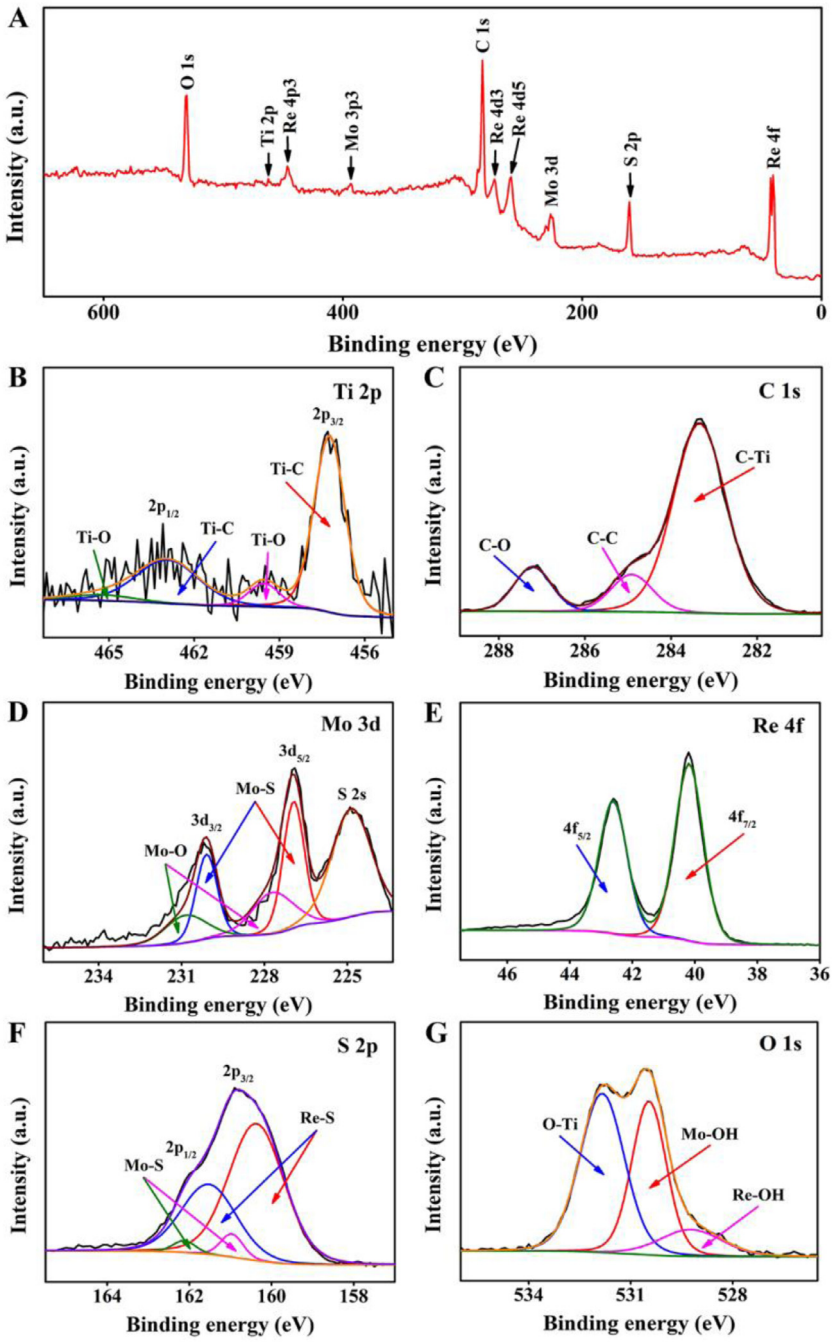

Fig. 2. XPS spectra of materials: (A) survey, (B) Ti 2p, (C) C 1 s, (D) Mo 3d, (E) *Re* 4f, (F) S 2p and (G) O 1 s.

lated E_{VB} and E_{CB} of MoS_2 were 1.54 eV and 0.11 eV, respectively, and the calculated E_{VB} and E_{CB} of ReS_2 were 1.8 eV and 0.04 eV, respectively. Since both electrons and currents were transferred from ReS_2 to MoS_2, the MoS_2@ReS_2 heterojunction was a type I heterojunction. Such heterojunction promoted the separation of electrons and holes, which was beneficial for enhancing the signal response. In addition, ReS_2 had a 1T structure and MoS_2 had a 2H structure, thus the large interface mismatch prolonged the recombination time of electron-hole. Because the conduction band of MoS_2 was higher than the Fermi energy level of Ti_3C_2 (vs. NHE) [34], the electrons could not be transferred to Ti_3C_2. Therefore, the mechanism of Ti_3C_2 to enhance the photocurrent response was through the rapid transfer of electrons to the GCE and the further hindrance of electron-hole recombination.

Moreover, we synthesized SiO_2–COOH and designed a composite probe system in order to achieve a higher signal output during photoelectric conversion. **Fig. S1A** shows the transmission electron microscopy (TEM) image of SiO_2. All particles were monodispersed with a size about 15 nm (**Fig. S1B**). **Fig. S1C** shows the Fourier transformed infrared spectra (FT-IR) of SiO_2 and SiO_2–COOH. As expected, the carboxyl vibration peak appeared at 1710 cm^{-1}, indicating the successful carboxylation [44]. Because the nucleic acid itself has a negative charge, the process of SiO_2 modification could make the zeta potential of SiO_2 more negative [45]. **Fig. S1D** shows that the zeta potentials of SiO_2, SiO_2-p2, and SiO_2-p2-p1 were −14.6, −15.8, and −35 eV, respectively, proving that the SiO_2 was successfully fixed in composite probe system. The signal amplification strategy based on composite probe system was illustrated in

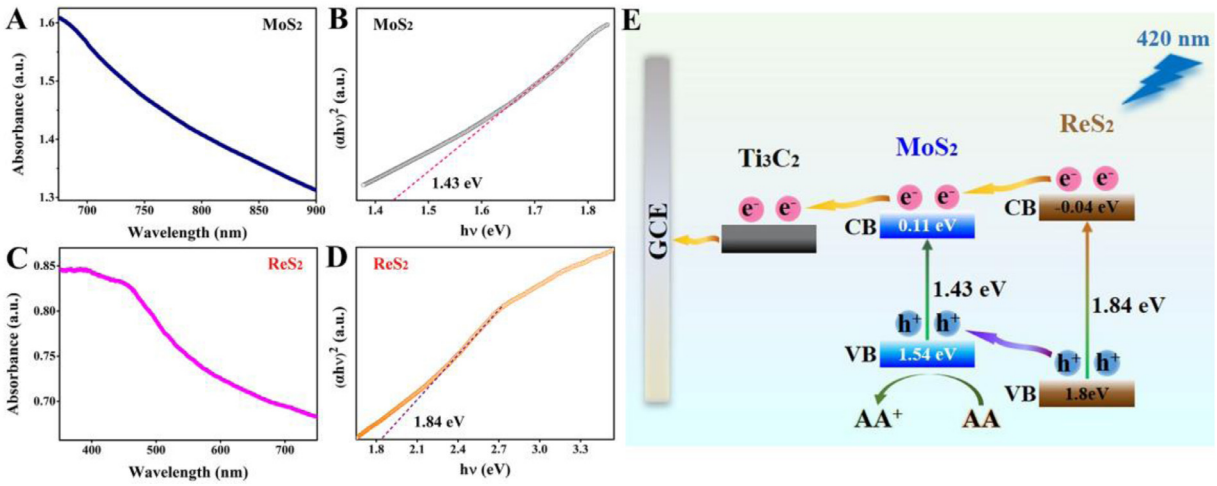

Fig. 3. Charge transfer mechanism of the PEC biosensing platform. UV–Vis absorption spectra (A, C) and Tauc plots (B, D) of MoS_2 and ReS_2. (E) Schematic illustration of the charge transfer mechanism of PEC biosensing platform.

Scheme 1 and further verified by polyacrylamide gel electrophoresis (**Fig. S3**). A previous study showed that DSN preserved the 12 nt of DNA at the miRNA-DNA junction, releasing 10 nt DNA Tc fragments [30]. The designed composite probe system with 8 complement base pairs would stay stable without piR-31,143 (**Fig. S3, lane 6**) which tellingly avoided false positives. The reaction process could be summarized as follows. At first, the charge transfer resistance was extremely high due to the strong steric hindrance effect. When piR-31,143 was present in solution, piR-31,143 would displace p2 of composite probe system through chain displacement reaction which removed the suppressive effect of SiO_2 (**Fig. S3, lane 7**). Subsequently, DSN specifically bound to piRNA-p1 complex and cleaved p1(**Fig. S3, lane 8**). The piR-31,143 template stayed intact and was recycled again and again, resulting in continuous amplification of the photocurrent signal and improving the sensitivity of detection.

3.3. Optimization of experimental conditions

To achieve higher detection sensitivity, we further optimized the experimental parameters including MoS_2:ReS_2 mass ratio, Ti_3C_2:MoS_2@ReS_2 mass ratio, Ti_3C_2/MoS_2@ReS_2 concentration, electrolyte pH, probe concentration and probe connection time. The photocurrent reached a peak when MoS_2:ReS_2 was 0.6 and Ti_3C_2:MoS_2@ReS_2 mass ratio was 0.35 (**Fig. S4A** and **B**). In addition, our results showed that the optimal Ti_3C_2/MoS_2@ReS_2 concentration to construct the electrode was 4 mg/mL (**Fig. S4C**). To investigate the effect of pH on the PEC response, the photocurrents were measured in buffer solutions with pH values from 3.5 to 8.5. The photocurrent reached the maximum when the pH value was 7.5 (**Fig. S4D**). Therefore, pH 7.5 was utilized in the following experiment. The probe concentration and binding time can also affect the PEC performance. The results indicated the optimal probe concentration was 0.1 μM, and the optimal binding time was 12 h (**Fig. S4E** and **F**).

3.4. Analytical characteristics of the PEC biosensor

The stepwise construction process of the PEC biosensing platform was confirmed by photocurrent and EIS analysis. **Fig. 4A** shows the PEC response of various modified electrodes. As shown in **Fig. S5**, under visible light, bare GCE exhibited powerless photocurrent reaction. Compared with the photocurrent of MoS_2 (I = 71.8 μA/cm^2, curve a), ReS_2 (I = 57.1 μA/cm^2, curve b), MoS_2@ReS_2 modified electrode showed an obviously increased photocurrent (I = 137.3 μA/cm^2, curve c), which could be attributed to the intrinsic photoactive capacity of the hybrid. Ti_3C_2 modified GCE exhibited relatively low photocurrent because the material itself produced fewer carriers (I = 24.5 μA/cm^2, curves d). The reason for the increased photocurrent of MoS_2@ReS_2/Ti_3C_2 was the higher conductivity of Ti_3C_2 (I = 219.2 μA/cm^2, curve e). When Au NPs were further assembled on MoS_2@ReS_2/Ti_3C_2 surface, the current further increased to 232.7 μA/cm^2 (curve f). Finally, after continuous immobilization of composite probe system (I = 75.8 μA/cm^2, curve g) and MCH (I = 65.1 μA/cm^2, curve h), photocurrent was gradually decreased because of the steric hindrance on the electrode, and it provided a low PEC background signal for the further detection of piR-31,143.

Furthermore, EIS analysis was applied to prove the assembly process of electrodes at different preparation stages. As revealed in **Fig. 4B**, the charge-transfer resistance (R_{CT}) of bare MoS_2 modified electrode was about 4214 Ω (curve a). Compared with bare ReS_2 modified electrode (R_{CT} ≈ 5407 Ω, curve b), MoS_2@ReS_2 hybrid largely enhanced electrical conductivity (R_{CT} ≈ 4650 Ω, curve b). On account of high electron transfer efficiency of Ti_3C_2 (R_{CT} ≈ 3028 Ω, curve b), MoS_2@ReS_2/Ti_3C_2 further reduced the R_{CT} (R_{CT} ≈ 3703 Ω, curve e). A lower RCT was achieved after the electrodeposition of Au NPs (R_{CT} ≈ 3557 Ω, curve f). Subsequently, a significant increase of the R_{CT} value was observed in the presence of composite probe system (R_{CT} ≈ 4298 Ω, curve g) and MCH (R_{CT} ≈ 4389 Ω, curve h), which was ascribed to their low conductivity caused by steric hindrance effect. In summary, all the results demonstrated the successful encapsulation of components.

The proposed biosensor was then used to detect various concentrations of the target. As shown in **Fig. 4C** and **D**, the photocurrent was increased gradually with the increased concentration of target within the range from 10^{-1} fM to 10^6 fM. The regression equation could be fitted as follows: y = 11.755* lgx + 86.14 (R^2=0.998). According to the 3σ method, the detection limit was calculated to be 23 aM. Meanwhile, the limit of quantification (LOQ) was estimated as the concentration of piR-31,143 that gives the signal equal to 10 standard deviations of the baseline noise [46], which was calculated to be 1.066 fM, suggesting that this PEC biosensor had the potential for ultrasensitive detection of piR-31,143. Our sensor exhibited a broader linear range and a lower detection limit compared with previously reported PEC biosensors (**Table S2**). Moreover, compared with other RNA liquid biopsy biosensors based on MoS_2 in **Table 1** and other CRC-specific miRNA

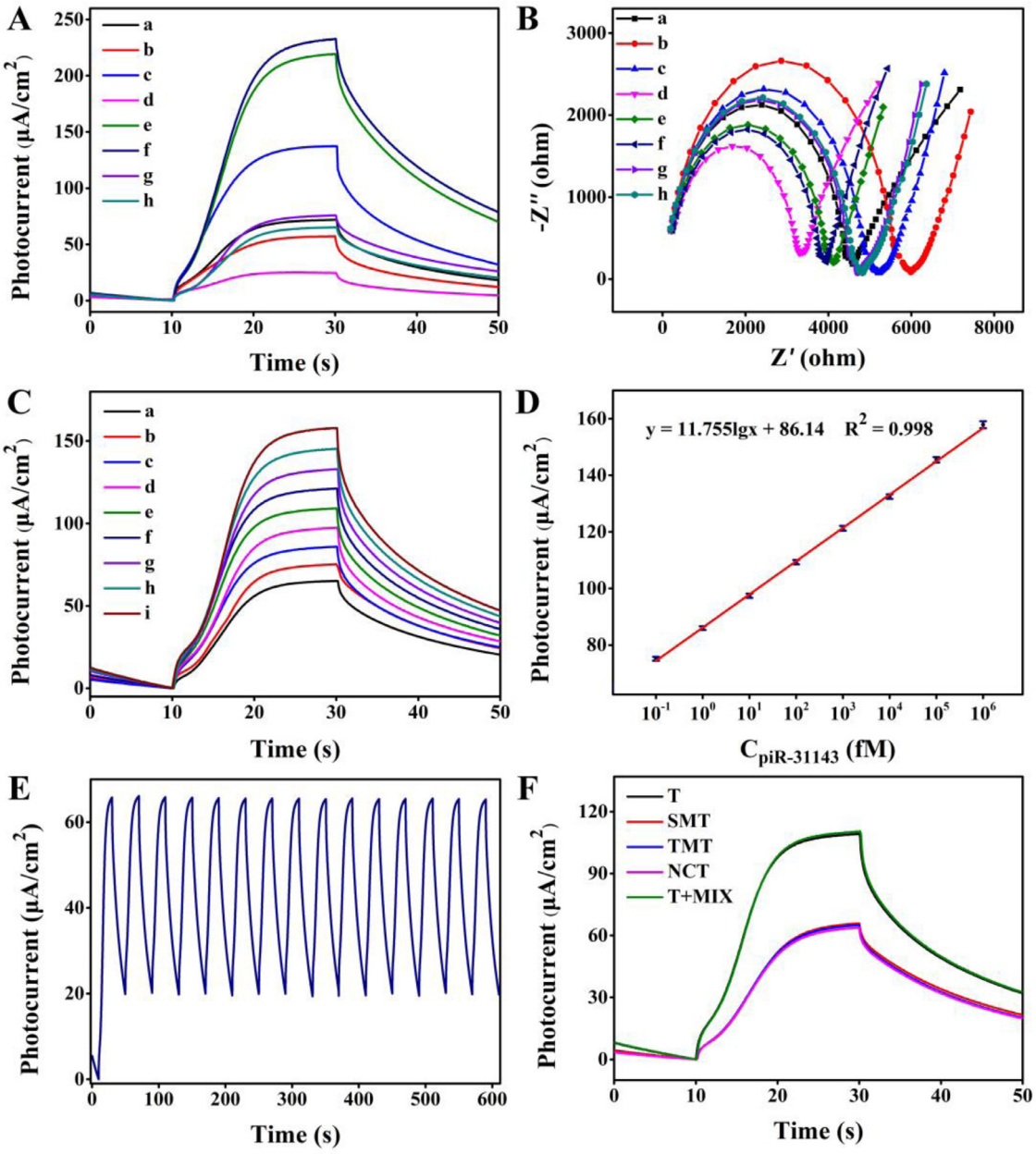

Fig. 4. Signal response and analytical performance of the PEC biosensor. Photocurrent (A) and EIS (B) of the PEC biosensor: (a) MoS_2/GCE, (b) ReS_2/GCE, (c) MoS_2@ReS_2/GCE, (d) Ti_3C_2/GCE, (e) MoS_2@ReS_2/Ti_3C_2/GCE, (f) Au NPs/MoS_2@ReS_2/Ti_3C_2/GCE, (g) probe/AuNPs/MoS_2@ReS_2/Ti_3C_2/GCE, (h) MCH/probe/Au NPs/MoS_2@ReS_2/Ti_3C_2/GCE. (C) Photocurrent of the PEC biosensor with different piR-31,143 concentrations. (D) Linear relationship between the photocurrent and the concentration of piR-31,143. (n = 3 repetitions) (E) Photocurrent of the PEC biosensor under 15 continuous radiation source on-off cycles. (F) Photocurrent of the PEC biosensor with different sequences.

Table 1
Comparison of biosensors for RNA detection based on MoS_2.

Nanomaterial	Type	Linear range (fM)	Detection limit (fM)	Ref.
3D MoS_2-rGO	ECL	$5 \sim 5 \times 10^8$	0.54	[47]
MoS_2 nanosheets	ECL	$1 \sim 10^5$	0.3	[48]
Bi_2S_3@MoS_2	ECL	$0.5 \sim 10^6$	2.65	[49]
Pl-Cys/MoS_2	ECL	$10^2 \sim 10^7$	78	[50]
(AuNPs)@MoS2	ECL	$1 \sim 10^7$	0.32	[51]
MoS_2 nanosheets	Optical	$10^4 \sim 2.5 \times 10^7$	6×10^3	[52]
MoS_2 QDs.	Optical	$5 \sim 5 \times 10^3$	4.6	[53]
MoS_2@Ti_3C_2	PEC	$1 \sim 10^8$	0.27	[34]
MoS_2@ReS_2/Ti_3C_2	PEC	$10^{-1} \sim 10^6$	0.023	This work

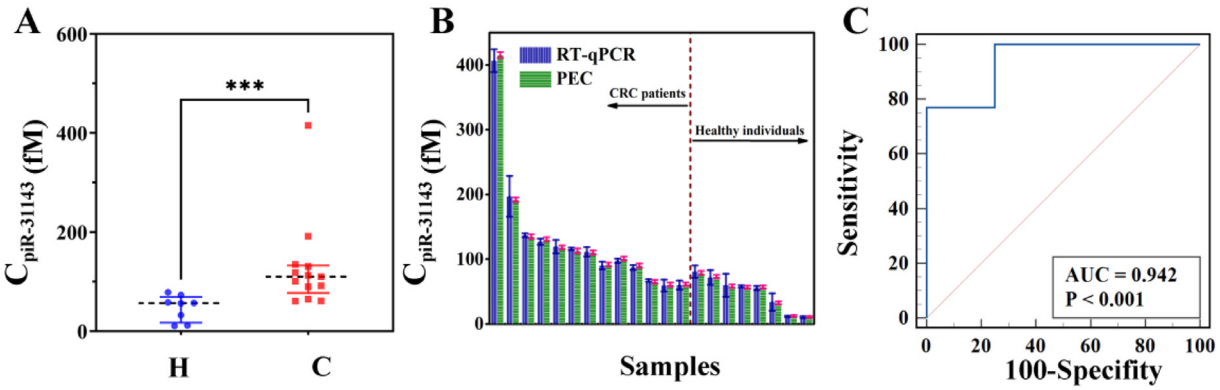

Fig. 5. Real sample analysis of PEC biosensor. (A) Quantification of piR-31,143 level in human serum samples from healthy controls and patients with colorectal cancer. H represents healthy control and C represents colorectal cancer patient. (B) Detection results of piR-31,143 concentration in clinical serum samples by RT-qPCR and PEC biosensor. (C) ROC curve to evaluate the diagnostic power of the PEC biosensor for colorectal cancer.

biosensors in **Table S3**, the PEC biosensor in this study still had the competitive advantage.

In this work, all tests were run three times in parallel and the reproducibility were represented by error bars. According to the results showed in **Fig. 4D**, all samples possessed standard deviations that less than 3%, demonstrating good reproducibility characteristics. The reproductivity of PEC biosensors mainly lies in the control of sensing layers on the substrates. In this work, we synthesized compounds rather than single elements to fabricate the biosensor and all of reagents and samples were sonicated for 5 min before used. In addition, GCE has a small enough work surface that makes compounds distribute evenly to keep the sensing layers consistent. Meanwhile, the stability of the PEC biosensor was verified by continuous scanning without target under "off-on-off" light for 15 cycles, and an RSD of 1.17% was observed (**Fig. 4E**), implying that the constructed biosensor possessed acceptable stability. The selectivity of the fabricated biosensor was evaluated by detecting target piRNA (100 fM) and mutation sequences (100 fM) including single mutation target (SMT), two mutations target (TMT), and non-complimentary target (NCT). As shown in **Fig. 4F**, the corresponding concentration of photocurrent of target piRNA was 101.6 fM. The other mutation sequences showed far lower fitting values than the 100 fM for the target, confirming that the biosensor had high selectivity for the detection of piR-31,143. In addition, the photocurrent of the mixture of sequences did not show much difference with the photocurrent of target piRNA, indicating our biosensor possessed high quantification ability in a complex sample.

In addition, we applied the PEC sensors in the analysis of serum samples and the standard PCR method was used to evaluate the accuracy of the biosensor (**Fig. S6**) [54]. In this study, we rinsed electrode with ultrapure water after the reaction and the PEC measurement was performed in the AA buffer [55–57]. As revealed in Fig. 5B, the obtained results had no obvious deviation between PCR and PEC sensors, demonstrating that the wash step could remove the effect of serum matrix sufficiently. Therefore, we considered that the analytical curves could be used to calculate the unknown concentration of piR-31,143 in serum samples. A total of 13 CRC patient samples and 8 healthy control samples were used to verify the differential expression of piR-31,143. Results showed that the serum piR-31,143 concentration of CRC patients was higher compared with healthy controls (**Fig. 5A**). In addition, this biosensor possessed large potential in the analysis of clinical samples (**Fig. 5B**). Furthermore, we investigated the diagnostic value of piR-31,143 using the ROC curve analysis and found that piR-31,143 had a significantly higher AUC value (0.942) with a 95% confidence interval ranging from 0.747 to 0.997(**Fig. 5C**). We found that 0.7692 was the highest Youden index J and the best cut-off value was 78.54. Under such circumstance, the sensitivity and specificity to distinguish cancer patients from healthy controls were 76.92% and 100%, respectively, which confirmed the reliable diagnostic ability of piR-31,143.

4. Conclusions

In summary, we successfully fabricated an advanced PEC biosensor for the ultrasensitive analysis of piR-31,143 using only 10 μL of serum by combining the DSN amplification strategy with MoS_2@ReS_2/Ti_3C_2 nanohybrid. The biosensor showed linear correlation between the photocurrents and the logarithm of piR-31,143 concentrations in a wider liner range from 10^{-1} fM to 10^6 fM and the LOD was down to 23 aM, compared with the previously reported biosensors. We also verified that the AUC of piR-31,143 was 0.942 with 100% specificity to distinguish CRC patients from healthy controls. Collectively, the PEC biosensor in this study provided a strategy for the diagnosis of colorectal cancer and had great application potential in clinical diagnosis. By transforming the recognition sequence of the probe, the sensor can be applied to a variety of piRNAs detection for different tumors. In addition, the electrode can be recycled which is beneficial to reduce the cost of detection. With suitable automation and further optimization, this biosensor may serve as core component in the development of an accurate and efficient CRC diagnosis method.

Declaration of Competing Interest

All authors declare that they have no conflicts of interest and no competing interest.

Acknowledgements

This research was supported by grant from the National Natural Science Foundation of China (81972007, 82130067, 52108287 and 82002228), Shandong Provincial Natural Science Foundation (ZR2020QH280), the Key Research and Development Program of Shandong Province (2019GHZ003 and 2020CXGC011304), Taishan Scholars Climbing Program of Shandong Province (NO.tspd20210323), Young Taishan Scholars Program of Shandong Province (NO.tsqn201909176), Qilu Young Scholars Program of Shandong University, Shandong Collaborative Innovation Center for R&D and Transformation of New Tumor Biomarkers Foundation (CXZX2019006), Tumor Biomarker Innovation Team Foundation of Jinan City (2019GXRC004), and Shandong University Clinical Research Project (2020SDUCRCA002).

Supplementary materials

Supplementary material associated with this article can be found, in the online version, at doi:10.1016/j.actbio.2022.06.037.

References

[1] S. Siddiqi, I. Matushansky, Piwis and piwi-interacting RNAs in the epigenetics of cancer, J. Cell. Biochem. 113 (2) (2012) 373–380.
[2] W. Weng, N. Liu, Y. Toiyama, M. Kusunoki, T. Nagasaka, T. Fujiwara, Q. Wei, H. Qin, H. Lin, Y. Ma, A. Goel, Novel evidence for a PIWI-interacting RNA (piRNA) as an oncogenic mediator of disease progression, and a potential prognostic biomarker in colorectal cancer, Mol. Cancer 17 (1) (2018) 16.
[3] L. Tan, D. Mai, B. Zhang, X. Jiang, J. Zhang, R. Bai, Y. Ye, M. Li, L. Pan, J. Su, Y. Zheng, Z. Liu, Z. Zuo, Q. Zhao, X. Li, X. Huang, J. Yang, W. Tan, J. Zheng, D. Lin, PIWI-interacting RNA-36712 restrains breast cancer progression and chemoresistance by interaction with SEPW1 pseudogene SEPW1P RNA, Mol. Cancer 18 (1) (2019) 9.
[4] D.M. Ozata, I. Gainetdinov, A. Zoch, D. O'Carroll, P.D. Zamore, PIWI-interacting RNAs: small RNAs with big functions, Nat. Rev. Genet. 20 (2) (2019).
[5] J.-.F. Su, F. Zhao, Z.-.W. Gao, Y.-.J. Hou, Y.-.Y. Li, L.-.J. Duan, S.-.M. Lun, H.-.J. Yang, J.-.K. Li, N.-.T. Dai, F.-.F. Shen, F.-.Y. Zhou, piR-823 demonstrates tumor oncogenic activity in esophageal squamous cell carcinoma through DNA methylation induction via DNA methyltransferase 3B, Pathol. Res. Pract. 216 (4) (2020) 152848.
[6] X. Ding, Y. Li, J. Lü, Q. Zhao, Y. Guo, Z. Lu, W. Ma, P. Liu, R.G. Pestell, C. Liang, Z. Yu, piRNA-823 Is Involved in Cancer Stem Cell Regulation Through Altering DNA Methylation in Association With Luminal Breast Cancer, Front. Cell Dev. Biol. 9 (2021) 641052.
[7] N.A. Sabbah, W.M. Abdalla, W.A. Mawla, N. AbdAlMonem, A.F. Gharib, A. Abdul-Saboor, A.S. Abdelazem, N. Raafat, piRNA-823 Is a Unique Potential Diagnostic Non-Invasive Biomarker in Colorectal Cancer Patients, Genes (Basel) 12 (4) (2021).
[8] N. Redshaw, T. Wilkes, A. Whale, S. Cowen, J. Huggett, C.A. Foy, A comparison of miRNA isolation and RT-qPCR technologies and their effects on quantification accuracy and repeatability, BioTechniques 54 (3) (2013) 155–164.
[9] M.N. Islam, V. Gopalan, M.H. Haque, M.K. Masud, M.S.A. Hossain, Y. Yamauchi, N.-.T. Nguyen, A.K.-Y. Lam, M.J.A. Shiddiky, A PCR-free electrochemical method for messenger RNA detection in cancer tissue samples, Biosens. Bioelectron. 98 (2017) 227–233.
[10] S.G. Jensen, P. Lamy, M.H. Rasmussen, M.S. Ostenfeld, L. Dyrskjøt, T.F. Orntoft, C.L. Andersen, Evaluation of two commercial global miRNA expression profiling platforms for detection of less abundant miRNAs, BMC Genomics 12 (2011) 435.
[11] M.K. Masud, M. Umer, M.S.A. Hossain, Y. Yamauchi, N.-.T. Nguyen, M.J.A. Shiddiky, Nanoarchitecture Frameworks for Electrochemical miRNA Detection, Trends Biochem. Sci 44 (5) (2019) 433–452.
[12] M.N. Islam, M.K. Masud, M.H. Haque, M.S.A. Hossain, Y. Yamauchi, N.-.T. Nguyen, M.J.A. Shiddiky, RNA biomarkers: diagnostic and prognostic potentials and recent developments of electrochemical biosensors, Small Methods 1 (7) (2017) 1700131.
[13] J. Shu, D. Tang, Recent advances in photoelectrochemical sensing: from engineered photoactive materials to sensing devices and detection modes, Anal. Chem. 92 (1) (2020) 363–377.
[14] L. Zhang, X.-.M. Shi, Y.-.T. Xu, G.-.C. Fan, X.-.D. Yu, Y.-.Y. Liang, W.-.W. Zhao, Binding-induced formation of DNAzyme on an Au@Ag nanoparticles/TiO nanorods electrode: stimulating biocatalytic precipitation amplification for plasmonic photoelectrochemical bioanalysis, Biosens. Bioelectron. 134 (2019) 103–108.
[15] Q. Zhang, L. Fu, Novel Insights and Perspectives into Weakly Coupled ReS2 toward Emerging Applications, Chem 5 (3) (2019) 505–525.
[16] Y. Zang, J. Lei, H. Ju, Principles and applications of photoelectrochemical sensing strategies based on biofunctionalized nanostructures, Biosens. Bioelectron. (2017) 96.
[17] Y. Li, J.G. DiStefano, A.A. Murthy, J.D. Cain, E.D. Hanson, Q. Li, F.C. Castro, X. Chen, V.P. Dravid, Superior Plasmonic Photodetectors Based on Au@MoS Core-Shell Heterostructures, ACS Nano 11 (10) (2017) 10321–10329.
[18] W. Wu, C. Wei, X. Lin, Q. Xu, Controlled Assembly of Porphyrin-MoS Composite Nanosheets for Enhanced Photoelectrochemical Performance, Chem. Asian J. 13 (10) (2018) 1293–1296.
[19] J. Cui, R. Jiang, W. Lu, S. Xu, L. Wang, Plasmon-Enhanced Photoelectrical Hydrogen Evolution on Monolayer MoS Decorated Cu S-Au Nanocrystals, Small 13 (8) (2017).
[20] Z. Yin, B. Chen, M. Bosman, X. Cao, J. Chen, B. Zheng, H. Zhang, Au nanoparticle-modified MoS2 nanosheet-based photoelectrochemical cells for water splitting, Small 10 (17) (2014) 3537–3543.
[21] B. Radisavljevic, A. Radenovic, J. Brivio, V. Giacometti, A. Kis, Single-layer MoS2 transistors, Nat. Nanotechnol. 6 (3) (2011) 147–150.
[22] W. Choi, M.Y. Cho, A. Konar, J.H. Lee, G.-.B. Cha, S.C. Hong, S. Kim, J. Kim, D. Jena, J. Joo, S. Kim, High-detectivity multilayer MoS(2) phototransistors with spectral response from ultraviolet to infrared, Adv. Mater. 24 (43) (2012) 5832–5836.
[23] M. Bernardi, M. Palummo, J.C. Grossman, Extraordinary sunlight absorption and one nanometer thick photovoltaics using two-dimensional monolayer materials, Nano Lett. 13 (8) (2013) 3664–3670.
[24] M.-.Y. Tsai, A. Tarasov, Z.R. Hesabi, H. Taghinejad, P.M. Campbell, C.A. Joiner, A. Adibi, E.M. Vogel, Flexible MoS2 Field-Effect Transistors for Gate-Tunable Piezoresistive Strain Sensors, ACS Appl. Mater. Interfaces 7 (23) (2015) 12850–12855.
[25] S.-.J. Ding, Z.-.J. Luo, Y.-.M. Xie, G.-.M. Pan, Y.-.H. Qiu, K. Chen, L. Zhou, J. Wang, H.-.Q. Lin, Q.-.Q. Wang, Strong magnetic resonances and largely enhanced second-harmonic generation of colloidal MoS and ReS@Au nanoantennas with assembled 2D nanosheets, Nanoscale 10 (1) (2017) 124–131.
[26] Y. Shi, L. Wang, X. Qiao, S. Li, Y. Liu, X. Li, X. Zhao, The Polarization Properties of the Reflection Spectra of Single-Layer MoS and ReS on SiO/Si and Quartz Substrates, Nanoscale Res. Lett. 15 (1) (2020) 43.
[27] J. Lv, J. Yang, S. Jiao, P. Huang, K. Ma, J. Wang, X. Xu, L. Liu, Ultrathin Quasibinary Heterojunctioned ReS/MoS Film with Controlled Adhesion from a Bimetallic Co-Feeding Atomic Layer Deposition, ACS Appl. Mater. Interfaces 12 (38) (2020) 43311–43319.
[28] C. Peng, X. Yang, Y. Li, H. Yu, H. Wang, F. Peng, Hybrids of Two-Dimensional Ti3C2 and TiO2 Exposing {001} Facets toward Enhanced Photocatalytic Activity, ACS Appl. Mater. Interfaces 8 (9) (2016) 6051–6060.
[29] Y. Kuang, J. Cao, F. Xu, Y. Chen, Duplex-Specific Nuclease-Mediated Amplification Strategy for Mass Spectrometry Quantification of MiRNA-200c in Breast Cancer Stem Cells, Anal. Chem. 91 (14) (2019) 8820–8826.
[30] E. Kim, P.D. Howes, S.W. Crowder, M.M. Stevens, Multi-Amplified Sensing of MicroRNA by a Small DNA Fragment-Driven Enzymatic Cascade Reaction, ACS Sens 2 (1) (2017) 111–118.
[31] Y. Zhang, P. Li, M. Hou, L. Chen, J. Wang, H. Yang, W. Feng, An electrochemical biosensor based on ARGET ATRP with DSN-assisted target recycling for sensitive detection of tobacco mosaic virus RNA, Bioelectrochemistry 144 (2021) 108037.
[32] L. Zhang, Z. Zhang, J. Xie, Y. Zhao, G. Tian, H. Jiang, H. Tao, J. Liu, Target invasion-triggered signal amplification based on duplex-specific nuclease for selective and sensitive detection of miRNAs, Anal. Chim. Acta 1189 (2022) 339182.
[33] Y. Zha, Y. Li, P. Hu, S. Lu, H. Ren, Z. Liu, H. Yang, Y. Zhou, Duplex-Specific Nuclease-Triggered Fluorescence Immunoassay Based on Dual-Functionalized AuNP for Acetochlor, Metolachlor, and Propisochlor, Anal. Chem. 93 (41) (2021) 13886–13892.
[34] Z. Sun, Y. Tong, L. Zhao, J. Li, F. Gao, C. Wang, H. Li, L. Du, Y. Jiang, MoS@TiC nanohybrid-based photoelectrochemical biosensor: a platform for ultrasensitive detection of cancer biomarker exosomal miRNA, Talanta 238 (Pt 2) (2022) 123077.
[35] M. Shang, Y. Gao, J. Zhang, J. Yan, W. Song, Signal-on cathodic photoelectrochemical aptasensing of insulin: plasmonic Au activated amorphous MoS photocathode coupled with target-induced sensitization effect, Biosens. Bioelectron. 165 (2020) 112359.
[36] F. You, J. Wei, Y. Cheng, Z. Wen, C. Ding, N. Hao, K. Wang, Selective and sensitive photoelectrochemical aptasensor for streptomycin detection based on BiVOBr/TiC nanohybrids, J. Hazard. Mater. 414 (2021) 125539.
[37] L. Liu, K. Ma, X. Xu, C. Shangguan, J. Lv, S. Zhu, S. Jiao, J. Wang, MoS-ReS Heterojunctions from a Bimetallic Co-chamber Feeding Atomic Layer Deposition for Ultrasensitive MiRNA-21 Detection, ACS Appl. Mater. Interfaces 12 (26) (2020) 29074–29084.
[38] S. Tongay, H. Sahin, C. Ko, A. Luce, W. Fan, K. Liu, J. Zhou, Y.-.S. Huang, C.-.H. Ho, J. Yan, D.F. Ogletree, S. Aloni, J. Ji, S. Li, J. Li, F.M. Peeters, J. Wu, Monolayer behaviour in bulk ReS2 due to electronic and vibrational decoupling, Nat. Commun. 5 (2014) 3252.
[39] X. Li, X. Lv, X. Sun, C. Yang, Y.-.Z. Zheng, L. Yang, S. Li, X. Tao, Edge-oriented, high-percentage 1T′-phase MoS2 nanosheets stabilize Ti3C2 MXene for efficient electrocatalytic hydrogen evolution, Appl. Catal. B: Environ. (2021) 284.
[40] L. Huang, L. Ai, M. Wang, J. Jiang, S. Wang, Hierarchical MoS2 nanosheets integrated Ti3C2 MXenes for electrocatalytic hydrogen evolution, Int. J. Hydrogen Energy 44 (2) (2019) 965–976.
[41] S. Zhang, B.V.R. Chowdari, Z. Wen, J. Jin, J. Yang, Constructing Highly Oriented Configuration by Few-Layer MoS2: toward High-Performance Lithium-Ion Batteries and Hydrogen Evolution Reactions, ACS Nano 9 (12) (2015) 12464–12472.
[42] X. Lu, R. Liu, Q. Wang, C. Xu, In Situ Integration of ReS/NiS p-n Heterostructure for Enhanced Photoelectrocatalytic Performance, ACS Appl. Mater. Interfaces 11 (43) (2019) 40014–40021.
[43] G. Swain, S. Sultana, J. Moma, K. Parida, Fabrication of Hierarchical Two-Dimensional MoS Nanoflowers Decorated upon Cubic CaInS Microflowers: facile Approach To Construct Novel Metal-Free p-n Heterojunction Semiconductors with Superior Charge Separation Efficiency, Inorg. Chem. 57 (16) (2018) 10059–10071.
[44] Y. Wang, F. Gayet, J.-.C. Daran, P. Guillo, D. Agustin, Replacement of Volatile Acetic Acid by Solid SiO@COOH Silica (Nano)Beads for (Ep)Oxidation Using Mn and Fe Complexes Containing BPMEN Ligand, Molecules 26 (18) (2021).
[45] S.S. Sahu, C. Stiller, E.P. Gomero, Á. Nagy, A.E. Karlström, J. Linnros, A. Dev, Electrokinetic sandwich assay and DNA mediated charge amplification for enhanced sensitivity and specificity, Biosens. Bioelectron. 176 (2021) 112917.
[46] A. Kausaite-Minkstimiene, A. Popov, A. Ramanaviciene, Surface Plasmon Resonance Immunosensor with Antibody-Functionalized Magnetoplasmonic Nanoparticles for Ultrasensitive Quantification of the CD5 Biomarker, ACS Appl. Mater. Interfaces 14 (18) (2022) 20720–20728.
[47] J. Dong, H. Yang, J. Zhao, L. Wen, C. He, Z. Hu, J. Li, D. Huo, C. Hou, Sandwich-type microRNA biosensor based on graphene oxide incorporated 3D-flower-like MoS and AuNPs coupling with HRP enzyme signal amplification, Mikrochim. Acta 189 (1) (2022) 49.

[48] J. Shi, Y. Zhang, P. Wang, Y. Nie, Q. Ma, Luminous MoS nanosheet-based electrochemiluminescence biosensor with biomimetic vesicle for miRNA-210 detection, Talanta 237 (2022) 122969.
[49] C. Zhou, K. Cui, Y. Liu, L. Li, L. Zhang, S. Hao, S. Ge, J. Yu, BiS@MoS Nanoflowers on Cellulose Fibers Combined with Octahedral CeO for Dual-Mode Microfluidic Paper-Based MiRNA-141 Sensors, ACS Appl. Mater. Interfaces 13 (28) (2021) 32780–32789.
[50] Y. Yao, H. Pan, Y. Luo, D. Zhu, J. Chao, S. Su, L. Wang, A label-free electrochemical sensor for ultrasensitive microRNA-21 analysis based on the poly(l-cysteine)/MoS sensing interface, Analyst 146 (5) (2021) 1663–1667.
[51] L. Liu, S. Zhu, Y. Wei, X. Liu, S. Jiao, J. Yang, Ultrasensitive detection of miRNA-155 based on controlled fabrication of AuNPs@MoS nanostructures by atomic layer deposition, Biosens. Bioelectron. 144 (2019) 111660.
[52] J. Wei, S. He, Y. Mao, L. Wu, X. Liu, C.Y. Effah, H. Guo, Y. Wu, A simple "signal off-on" fluorescence nanoplatform for the label-free quantification of exosome-derived microRNA-21 in lung cancer plasma, Mikrochim. Acta 188 (11) (2021) 397.
[53] J. Ge, Y. Hu, R. Deng, Z. Li, K. Zhang, M. Shi, D. Yang, R. Cai, W. Tan, Highly Sensitive MicroRNA Detection by Coupling Nicking-Enhanced Rolling Circle Amplification with MoS Quantum Dots, Anal. Chem. 92 (19) (2020) 13588–13594.
[54] M.N. Islam, M.K. Masud, N.-.T. Nguyen, V. Gopalan, H.R. Alamri, Z.A. Alothman, M.S.A. Hossain, Y. Yamauchi, A.K. Lamd, M.J.A. Shiddiky, Gold-loaded nanoporous ferric oxide nanocubes for electrocatalytic detection of microRNA at attomolar level, Biosens. Bioelectron. 101 (2018) 275–281.
[55] X. Niu, Y. Zhao, F. Wang, J. Wu, F. Qu, W. Tan, Ultrasensitive Photoelectrochemical Biosensor Based on Novel Z-Scheme Heterojunctions of Zn-Defective CdS/ZnS for MicroRNA Assay, Anal. Chem. 93 (51) (2021) 17134–17140.
[56] Y. Zhao, J. Xiang, H. Cheng, X. Liu, F. Li, Flexible photoelectrochemical biosensor for ultrasensitive microRNA detection based on concatenated multiplex signal amplification, Biosens. Bioelectron. 194 (2021) 113581.
[57] F. Mo, J. Guo, M. Chen, H. Meng, Y. Fu, Gold Nanoparticles Photosensitization towards 3,4,9,10-Perylenetetracarboxylic Dianhydride Integrated with a Dual–Particle Three-Dimensional DNA Roller: a General "ON-OFF-ON" Photoelectric Plasmon-Enhanced Biosensor, Anal. Chem. 93 (31) (2021) 10947–10954.